Internal tides off the Amazon shelf in the western tropical Atlantic: Analysis of SWOT Cal/Val Mission Data

Michel Tchilibou[1], Loren Carrere[1], Florent Lyard[2], Clément Ubelmann[3], Gérald Dibarboure[4] , Edward D. Zaron[5], and Brian K. Arbic[6]

[1] Collecte Localisation Satellites, 31520 Ramonville-Saint-Agne, France

[2] Université de Toulouse, LEGOS (CNES/CNRS/IRD/UT3), 31400 Toulouse, France

[3] Datlas, Grenoble, France

[4] Centre National d'Etude Spatiales, 31400, Toulouse, France

[5] College of Earth, Ocean and Atmospheric Science, Oregon State University, Corvallis, OR, USA

[6] Department of Earth and Environmental Sciences, University of Michigan, Ann Arbor, MI, USA

Correspondence to: Michel Tchilibou (mtchilibou@groupcls.com)

Abstract

This study focuses on the internal tides (IT) off the Amazon shelf in the tropical Atlantic. It is based on 2 km horizontally gridded observations along the swaths of SWOT (Surface Water and Ocean Topography) track 20 during the calibration/validation phase (Cal/Val, 1-day orbit) from late March to early July 2023. We evaluate the amplitude of M_2, N_2 and S_2 frequencies and use the M_2 atlas as an internal tide correction model for SWOT observations. Internal tide amplitudes (models or atlases) are first derived by harmonic analysis of the SWOT sea level anomaly (SLA). The estimation is improved by performing a principal component analysis (PCA) before the harmonic analysis. The results compare very well with the high-resolution empirical tide (HRET) internal tide model, the reference product for internal tide corrections in altimetry observations. The coherent mode 1 and mode 2 M_2 tides can be distinguished in the internal tide model derived from SWOT, while the higher modes with their strong SLA signature are seen mostly in the incoherent part. In comparison to HRET, the correction of SWOT observations with SWOT-based atlases may be more relevant for this track.

Introduction

The launch of the SWOT mission at the end of 2022 certainly marks a new phase in spatial altimetry. SWOT is equipped with the KaRIn instrument, a Ka-band radar interferometer capable of measuring the sea surface topography with unprecedented resolution in two-dimensional swaths. KaRIn consists of two antennae that take 2D measurements in two 50 km-wide swaths separated by a 20 km gap covered by the conventional nadir radar altimeter also carried by the mission. The accuracy of SWOT's instruments is such that SWOT should be able to observe the ocean down to a spatial scale of 15-30 km (Morrow et al., 2019; Dufau et al., 2016; Wang et al., 2019), thus, complementing our 2D view of the ocean with Topex/Poseidon class nadir altimetry, which is limited to scales larger than 150 km (Chelton et al., 2011; Ballarotta et al., 2019) along one-dimensional tracks rather than two-dimensional swaths. The main oceanographic objective of the SWOT mission is to characterize mesoscale and sub-mesoscale ocean circulation (Fu et al., 2012; Fu and Ubelmann, 2014). However, ocean processes at the scales targeted by SWOT (150-15 km) encompass both "balanced" geostrophic motions, as well as surface and internal inertia-gravity waves at tidal frequencies. The correction of internal tides (IT) surface signatures presents a significant challenge to the useability of SWOT data, considering that the

40 spatial scales of these waves overlap with those of balanced motions. Conversely, the exploitation of
41 SWOT data to study IT is an opportunity for learning more about these waves and quantifying their
42 impacts in the ocean.

43 Efforts have been made in recent years to map internal tides using conventional altimetry
44 observations. This was made possible by the fact that the internal tide has a SSH (Sea Surface height)
45 signature of the order of one to several centimeters (Ray and Mitchum, 1997). However, the coarse
46 sampling in both space and time of conventional altimetry is a hindrance. To derive spatially
47 continuous high-resolution maps of the internal tide SSH from the sparse altimeter sampling, Dushaw
48 (2015), Zhao et al. (2019) and Zaron (2019) used least-squares techniques to fit kinematic wave
49 solutions to nadir altimetry. Ubelmann et al., (2022) proposed jointly estimating internal tides and
50 mesoscale eddies to produce 2D maps of internal tides from conventional altimetry observations. The
51 advent of SWOT presents an opportunity to validate these internal tide maps using direct 2D
52 observations of the ocean. However, there is still some debate about the extraction of the internal
53 tidal signal along SWOT swaths. The first objective of our study is thus to estimate the internal tidal
54 signal along the SWOT swaths. Le Guillou et al., (2021) propose a data assimilation method coupled
55 with a simple dynamical model to separate internal tides and balanced motion in SWOT data. The
56 possibility of using deep learning to access internal tide signals is raised by Wang et al. (2022). Without
57 questioning these methods, we will show that classical methods of harmonic analysis and principal
58 component analysis (PCA) can be used to obtain internal tide maps from SWOT data.

59 Following the linear theory of ocean vertical modes, internal tides can be decomposed as a sum of
60 orthogonal baroclinic modes (Gill, 1982; Kelly et al., 2016). The first modes (mode 1 and mode 2)
61 propagate over hundreds or even thousands of kilometers. Higher modes have much shorter
62 wavelengths and are likely to dissipate close to the internal tide generation site, due to their low group
63 velocity and high shear (St Laurent and Garrett, 2002; Vic et al.,2019) and therefore could barely be
64 observed in classical nadir altimetry observations. In practice, the internal tide is separated into the
65 so-called coherent and incoherent internal tides. The coherent internal tide is the part of the internal
66 tide which remains phase-locked with the generating barotropic tide over an arbitrary period and is
67 easily obtained by harmonic analysis over the targeted period. Consequently, the residual that escapes
68 harmonic analysis constitutes the incoherent internal tide. The amplitude, phase, and trajectory of
69 incoherent internal tide results from refraction, reflection, and advection of internal tide by the ocean
70 background circulation including eddies, currents, and stratification (Ponte and Klein, 2015; Nelson et
71 al.,2019; Buijsman et al., 2017; Dunphy et al., 2017; Dunphy and Lamb, 2014; Duda et al., 2018; Savage
72 et al., 2020; Barbot et al., 2021). The incoherency of the internal tide makes it difficult to correct for in
73 altimetry observations. In the SWOT data processing protocol (Dibarboure et al.,2024), the coherent
74 part of the internal tide is corrected using the HRET (High-Resolution Empirical Tide) model of Zaron
75 (2019). The second objective of this study thus concerns the correction of the coherent internal tide in
76 the SWOT data: between HRET (the reference model) and the internal tide estimates directly on SWOT,
77 which is most relevant for correcting the internal tide on SWOT data?

78 Like the barotropic tides, the internal tides are a mixture of long- and short-period waves, among
79 which are the main astronomical tides, such as the diurnal waves (O1, K1, P1) and the semi-diurnal
80 waves (M2, S2, N2, K2). Due to the long repeat cycles of altimetry satellites, short tidal periods are
81 aliased to longer periods (Le Provost, 2001). The M2 tide, for example, is aliased to 62.11 days for the
82 TOPEX/Jason 10-day orbit (9.92 days precisely). With SWOT sampling, M2 is aliased to 66.02 days or
83 12.35 days (Table 1), depending on whether we consider the 21-day final science orbit or the 1-day
84 calibration/validation (Cal/Val) orbit (0.99343 days exactly). Table 1 gives an overview of the aliasing
85 periods of the main diurnal and semi-diurnal tidal frequencies on the SWOT Cal/Val orbit. Table 1 is

completed by the Rayleigh criterion values which provide information on the duration of the records needed to separate the different waves. SWOT was maintained in its Cal/Val orbit for about 6 months, providing slightly more than 3 months of usable data from March to early July 2023. Our study is based on this unprecedented 1-day orbit database and concerns observations along a single SWOT track in the Atlantic Ocean.

Table 1: Period of aliasing (in days, second line) and separability following the Rayleigh criterion (in days, from the third line to the end) of main tidal waves for SWOT's 1-day orbit.

	M2	S2	N2	K2	O1	P1	K1	Sa	Ssa
Periods	12.35	75.60	8.53	129.01	12.97	106.94	258.03	365.26	182.62
M2	--------	14.77	27.55	13.66	258.03	13.97	12.97	12.79	13.25
S2	--------	----------	9.61	182.62	15.66	258.03	106.94	95.34	129.01
N2	-------	-------	--------	9.13	24.9	9.27	8.82	8.73	8.95
K2	--------	-------	--------	--------	14.42	624.89	258.03	199.47	439.51
O1	-------	--------	--------	-------	---------	14.77	13.66	13.45	13.97
P1	-------	--------	--------	-------	--------	---------	182.62	151.20	258.03
K1	--------	--------	--------	-------	------	--------	---------	878.92	624.89
Sa	--------	--------	--------	------	--------	-------	-----	----------	365.22

This study focuses on the Cal/Val track 20 off the Amazon shelf in the western tropical Atlantic between 2°S and 15°N (Figure 1). The track has been chosen because the Amazon shelf is one of the hot spots for internal tide generation in the ocean (Arbic et al., 2012; Solano et al. 2023; Niwa and Hibiya et al., 2011). The region is marked by strong seasonal cycles of stratification, circulation and eddies that regulate the generation and propagation of internal tides (Barbot 2021, Tchilibou et al., 2022). The stratification is modulated by freshwater inflows from precipitation (under the inter-tropical convergence zone) and rivers (Amazon and Para rivers). The strong western boundary current, the North Brazil Current (NBC), controls the extension of the Amazon's plume and develops a double retroflexion into the Equatorial UnderCurrent (EUC, around 2°S-2°N) and the North Equatorial CounterCurrent (NECC, around 5°N-8°N). The barotropic and baroclinic instabilities of these currents generate some of the eddies present in the region (Aguedjou et al., 2019). Internal tides generated between the isobaths 100 and 2000 m along the shelf break propagate mainly from the six sites indicated in Figure 1 (Tchilibou et al.,2022; Assene et al., 2024). Between March and July, the pycnocline is shallow, the mesoscale activity and currents are low, consequently, internal tides tend to keep more coherent (Tchilibou et al., 2022). During the rest of the year, the pycnocline is deeper, mesoscale and currents are strong, and, consequently, the incoherence of internal tides increases as their reflection and advection by the circulation intensifies. As they evolve, internal tides disintegrate into nonlinear internal solitary waves (Jackson et al., 2012; Alford et al., 2015; Egbert and Erofeeva 2021). Packets of nonlinear internal solitary waves (ISWs) have been reported along the Amazon continental shelf and offshore (Lentini et al., 2016; Bai et al., 2021, Brandt et al., 2002; Magalhães et al., 2016). They are highly active in the area (4-8°N /40-45°W, see Figure 2 of de Macedo et al., 2023) of concentration of internal tides rays emanating from sites A and D, and they have a seasonal cycle of occurrence and wavelengths in agreement with those of internal waves (de Macedo et al., 2023).

The orientation of SWOT track 20 in this part of the ocean is such that it intersects three areas with potentially different dynamics (Tchilibou et al., 2022). Between 2.5°S and 2.5°N (area 1, Figure 1), the track is in the path of internal tides generated at points B, C and, to a lesser extent, A. In area 2, between 2.5°N and 8°N (Figure 1), the track crosses the zone of interaction between internal tides and mesoscale. Finally, area 3, north of 10°N (Figure 1), lies on the mid-Atlantic Ridge, where some IT can likely be generated also. We will keep all this in mind when interpreting our results.

124   The paper is structured as follows: The data used, the evidence for the presence of internal tides in
125   the SWOT data and the variability of the SLA at different scales are presented in section 1. The
126   amplitude of the internal tides is first estimated from the SWOT data in section 2. In section 3, the
127   estimation of internal tides is improved by introducing PCA. The SWOT based internal tide models and
128   HRET are further compared in section 4. The paper ends with a conclusion and discussion.

129
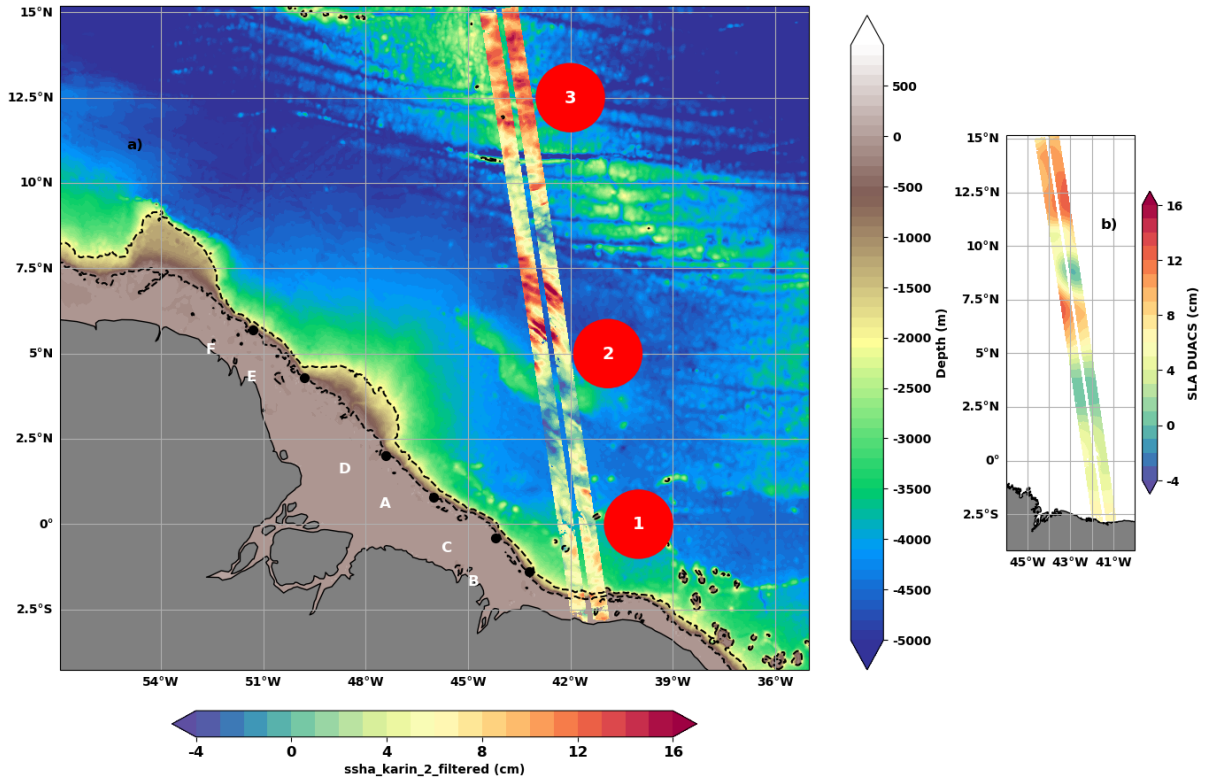
Figure 1: a) Bathymetry (m) off the Amazon shelf in the western tropical Atlantic. SLA KaRin (cm) on
08 April, 2023, along track 20 of SWOT's 1-day cycle. The main internal tide generation sites are marked
by the letters A to F. The 200 and 2000 m isobaths are dotted. The circles locate area 1 (2.5°S to 2.5°N),
area 2 (2.5°N to 8°N) and area 3 (north of 10°N) along the track. b) large scale structure from DUACS
at the same date.

1- Data and Variability: Evidence of IT propagation at different scales

1.1- Description of the database:

137   We use version V0.3 of the L3 SWOT products, released in December 2023. The data, made up of
138   several variables, are provided on regular horizontal grids of 2 km by 2 km. Using the naming
139   convention used in the dataset, we have defined the SLA by equation 1 below:

140   SLA = ssha_karin_2_filtered+ internal_tide_hret - duacs_ssha_karin_2_oi,   (1)

141   The first term on the right, 'ssha_karin_2_filtered' (the same as ssha_noiseless), is the SWOT
142   observation at the two KaRIn swaths only. We exclude SWOT nadir observations, to focus on the
143   SWOT's potential to observe directly 2D maps of the ocean. The ssha_karin_2_filtered has been
144   denoised using data-driven machine-learning noise reduction and corrected from all the classic
145   physical, instrumental and environmental corrections applied in altimetry (Dibarboure et al. 2024). The
146   tidal corrections applied are FES2022 model (Lyard et al., personal communication; Lyard et al., 2021)

147 for the barotropic tide and HRET for the internal tide (Zaron, 2019). We reintroduced HRET's internal
148 tide SSH (internal_tide_hret), so that our final SLA contains the total internal tide signal. The last term
149 'duacs_ssha_karin_2_oi' corresponds to the DUACS Maps of Sea Level Anomaly (MSLA) interpolated
150 on SWOT swaths (Ballarotta et al., 2023; Ubelmann et al. 2015, 2021). It removes the large-scale ocean
151 signals and particularly the mesoscale eddies that can mask internal waves at these latitudes. On track
152 20, we have the SLA from March 29 to July 10, 2023, i.e. 104 cycles with completely or partially filled
153 swaths. We have removed the mean SLA from the entire Cal/Val mission.

154 We recall that HRET is an empirical estimate of the internal tides at the M2, S2, K1 and O1
155 frequencies. The variable internal_tide_hret in the SWOT data and HRET model in this paper refers to
156 the HRETv8.1 version (Zaron, 2019). This version was developed by analyzing 25 years (1993-2017) of
157 exact-repeat mission altimetry including the TOPEX/Poseidon-Jason missions, the ERS-Envisat-AltiKa
158 missions and the GEOSAT Follow-On mission. The implementation of HRET involves a local two-
159 dimensional Fourier analysis of the along-track data, and the determination of the coefficients of a
160 spatial model by weighted least-squares fitting (second order polynomials fitting). The estimated tidal
161 fields are gridded on a regular latitude-longitude grid by weighted averaging, and a mask is used to set
162 the values to zero in regions where the estimate is too noisy. HRET includes mode 1 and mode 2
163 internal tides, but mode 2 is very weak in the present study area.

164 **1.2- Evidence of IT propagation at different scales:**

165 The snapshots in Figure 2a show very fine-scale crest-like structures superimposed on positive and
166 negative SLA spaced tens and hundreds of kilometers apart. The scenario repeats itself on the other
167 cycles (see movie in the supplementary material), indicating that SWOT likely sees internal waves of
168 different spatial scales. We submitted the SLA to spectral analysis to learn more about its frequency
169 and wavelength. The 2D FFT spectra are computed in the time (cycles) and along-track (latitude)
170 dimensions and then averaged over the cross-track (longitude) dimension. The Tukey 0.25 window is
171 used for windowing. The wavenumber-frequency (Figure 3a) was integrated to derive the
172 wavenumber spectrum (Figure 3b) and the frequency spectrum (Figure 3c).

173
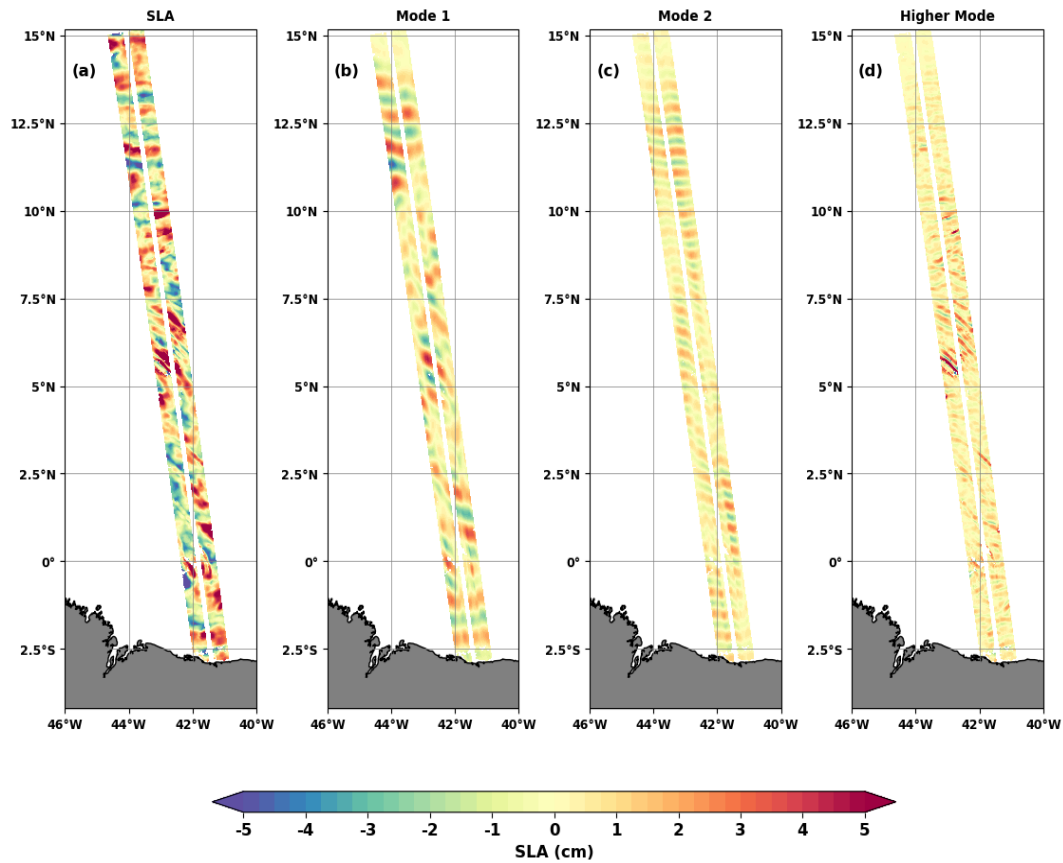
Figure 2: Snapshot of SWOT SLA on April 8, 2023. a) Total SLA, b) Mode 1 FFT-filtered SLA (180-90 km), c) Mode 2 FFT-filtered SLA (80-60 km) and d) Higher mode FFT-filtered SLA (50-2 km).

176

177   The wavenumber-frequency (Figure 3a), the wavenumber (Figure 3b) and the frequency (Figure 3c)
178   spectra of SWOT SLA indicate that the dominant signal is M2 aliased to 12.22 days (see Table 1). At
179   the M2 aliased frequency, the energy is greatest between 180-90 km and between 80-60 km (Figure
180   3a), leading to the spectral peaks in Figure 3b. These two wavelength bands correspond well to the
181   theoretical baroclinic mode 1 and 2 scales expected for the internal tide in this region (Zhao, 2021).
182   We isolated the SLA for these two wavelength bands using FFT filtering. When filtering, the FFT is
183   calculated on the along-track dimension. Snapshots of the Mode 1 and Mode 2 SLA are shown in
184   Figures 2b and 2c for the same day as Figure 2a, revealing more of the SLA's wave-like behavior.

185   Figure 2d shows the FFT-filtered SLA between 50-2km. This band contains all the small-scale
186   structures, including the very remarkable and intense one that appears as wave crests on the SLA. On
187   the wavenumber-frequency spectrum (Figure 3a), the energy maximum at frequency M2 extends to
188   scales smaller than 50 km. According to Barbot et al., (2021), this could be associated to internal tide
189   of mode 3, mode 4 and mode 5. We therefore consider the 50-2 km band as consisting of higher
190   modes.

191
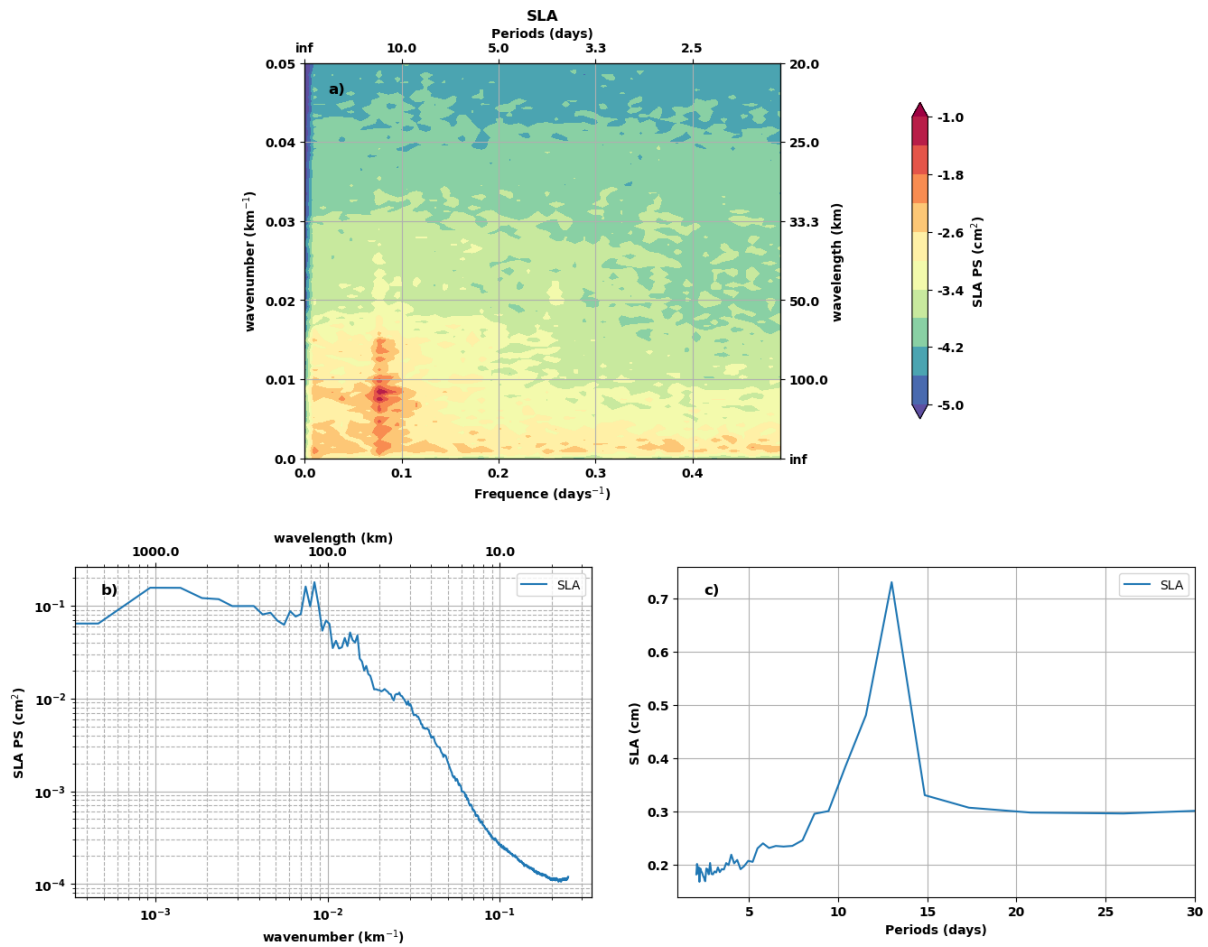
Figure 3: Wavenumber-frequency (a), wavenumber (c) and frequency (d) spectra of the total SLA.

1.3- Variability analysis of IT observations:

Analyses of SLA variability are completed by calculating the standard deviations of the total and the spatially FFT-filtered SLAs in the wavelength bands defined above. Over the Cal/Val period, SLA varies between 1 and 5 cm under track 20 (Figure 4a). Apart from the area very close to the coastline, there are three main patches of maximum variability, each located in one of the dynamic areas highlighted in the introduction. The maximum variability of the SLA in area 1 (2.5°S-2.5°N) is mainly due to the regular mode 1 internal tide flux likely coming from sites A, B and C (Figure 4b). Mode 2 and higher modes contributions are secondary (Figures 4c and 4d) in area 1. Higher modes have a major impact on the variability in area 2 where they make the SLA vary by 2 to 3 cm (Figure 4d), i.e. almost of the same order as mode 1 in the same area. As area 2 is far from the generation sites of the Amazonian shelf-break, the higher modes here are likely to originate from desintegration of mode 1 and mode 2. In area 3, SLA variability is driven mainly by mode 1 and mode 2.
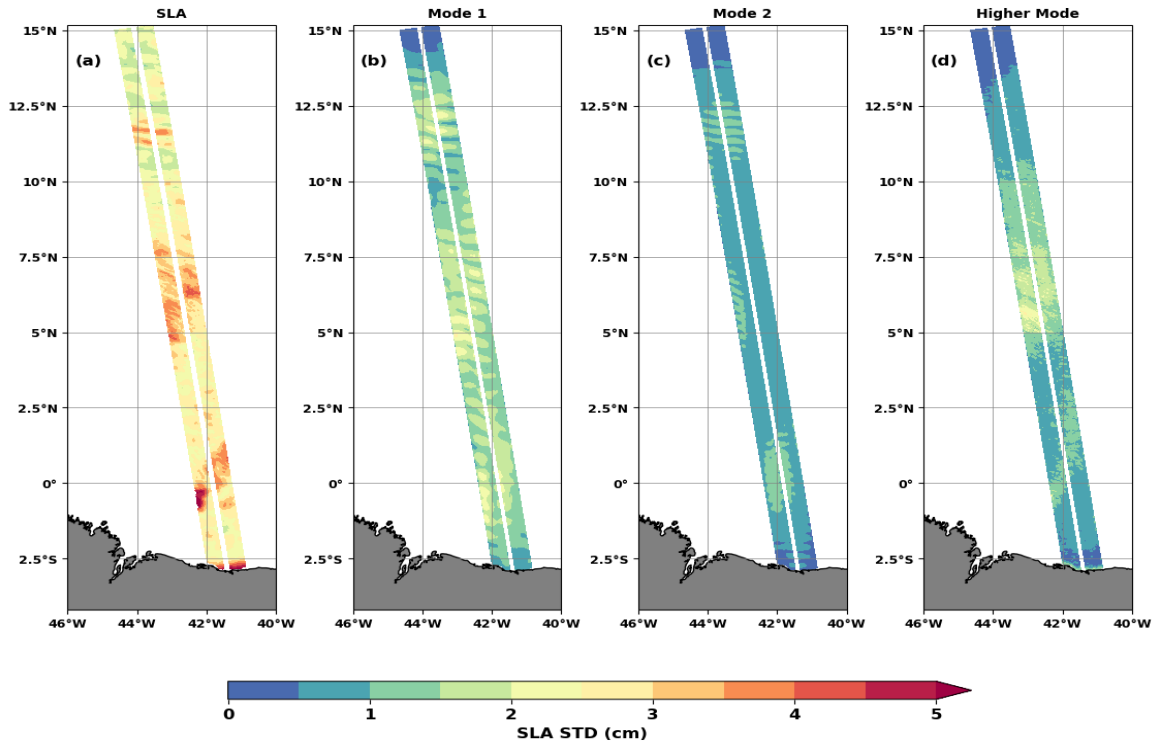
Figure 4: Standard deviation (in cm) of the total (a) SLA, and mode 1(b), mode 2 (c) and higher mode (d) FFT-filtered SLA.

2- The M2, S2 and N2 coherent internal tides from SWOT: ITkars model

In Table 1, 4 waves (M2, N2, S2, and O1) have aliasing periods shorter than the 104 days corresponding to the total length of our SWOT SLA series and are a priori of interest for our analysis. But given the Rayleigh criterion between them in Table 1, it is reasonable to restrict ourselves to the three semi-diurnal waves. Harmonic analysis based on least-squares fitting is used to extract the coherent internal tide at each band point with at least 80 valid cycles over the entire SWOT Cal/Val observation period. In the following, ITkars (IT from KARin Swot) refer to SWOT estimation of IT.
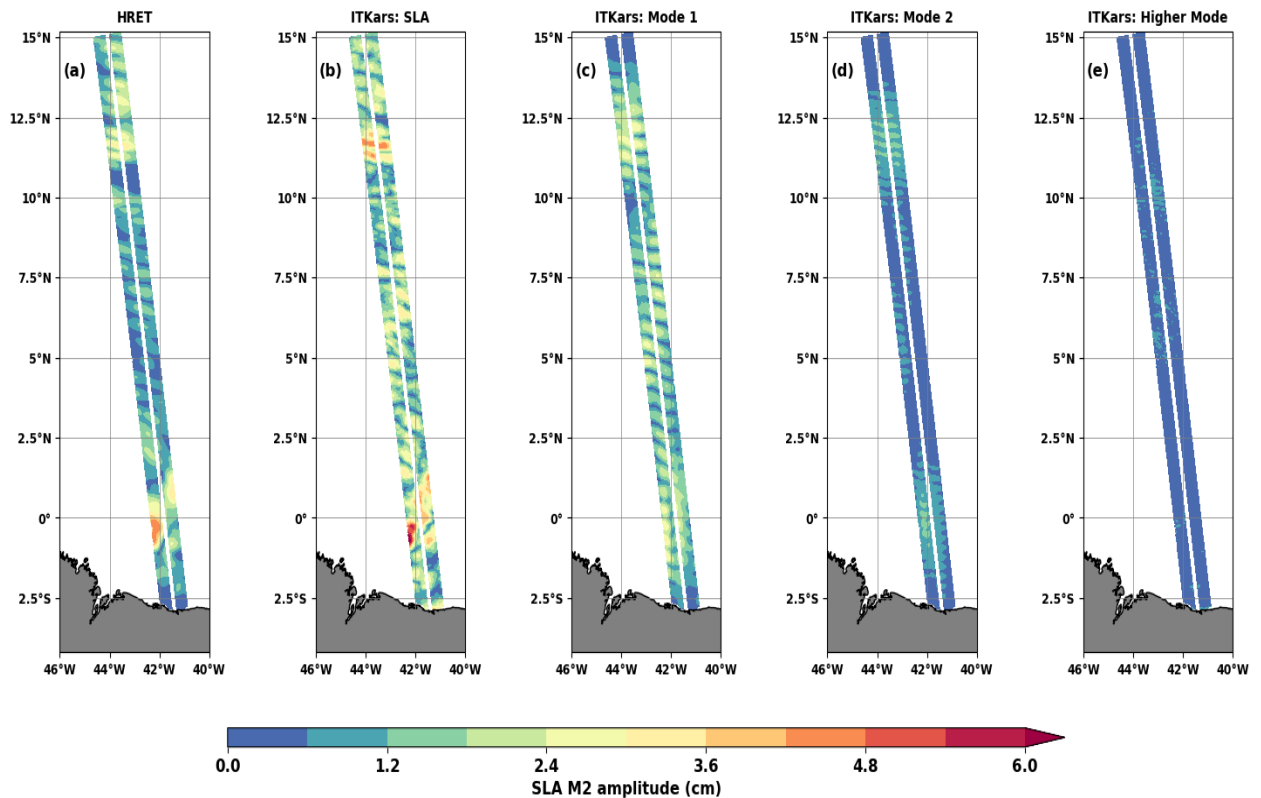
Figure 5: The amplitude (in cm) of the M2 internal tide from the HRET model (a) and the ITkars (b to e) model over the cal/val period. ITkars is derived by harmonic analysis of the total SWOT SLA (b) and FFT-filtered SWOT SLA for mode 1 (c), mode 2 (d) and higher mode (e) SLA. Only swath points with at least 80 valid cycles were analyzed.

The amplitudes of the coherent internal tide at the M2 frequency are presented in Figure 5 for both HRET (which include mostly mode 1 on this area) and ITkars models (which include mode 1 and mode 2). We first performed the harmonic analysis of the total SLA (Figure 5b) and repeated the harmonic analyses for each of the FFT-filtered SLAs (Figure 5c to e). The HRET model (Figure 5a) and the ITkars model based on the total SLA (Figure 5b) are similar in terms of spatial distribution, but as expected HRET has smoother and lower amplitudes because it represents a mean on many years of altimetry data. In areas 1 and 3, ITkars shows spatial features identical to those already observed on the standard deviation in Figure 4a. So, the maximum variability for these two parts of the SWOT track is indeed due to the M2 coherent internal tide. The discrepancies between standard deviations (Figure 4) and internal tide amplitudes (Figure 5) are best seen by directly comparing the maps for the different modes or wavelength bands. In area 2, the amplitude of the coherent internal tide is less than 1.5 cm for the higher modes (Figure 5e), whereas at these scales the standard deviation is maximal (Figure 4d). The high variability of the SLA found in area 2 is evidently related to internal tide incoherency.

As S2 from HRET shows unexpected patterns (not shown) and, and N2 is not available in HRET,we show only ITkars results in Figure 6. Both waves have smaller amplitudes than M2 and do not have the same structure as the latter. As the semi-diurnal S2 and N2 IT should have similar patterns to M2, those results indicate that these frequencies are certainly contaminated by other tidal waves due to poor separability on the available period (see Table 1) and are likely also contaminated by the mesoscale. Can we hope to improve our estimate of the coherent internal tide from SWOT observations?
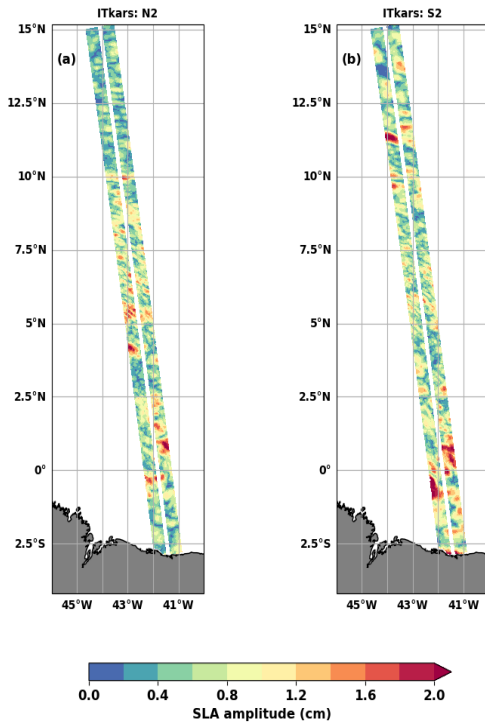
Figure 6: The amplitude (in cm) of the N2 (a) and S2 (b) internal tide of the ITkars model derived by harmonic analysis of the total SLA over the Cal/Val period. Only swath points with at least 80 valid cycles were analyzed.

3- An attempt to improve the estimation of coherent internal tide from SWOT Cal/Val data: Using principal component analysis (PCA) to separate SLA content

3.1- Separation using PCA

PCA, also known as EOF (Empirical Orthogonal Function), is a statistical analysis technique for reducing the dimensionality of a data set (Jolliffe, 1986). Applied to geophysical data, PCA separates the total signal into independent spatial patterns associated with independent temporal components (Principal Component) and gives a measure of the relative importance of each pattern (a percentage of the total variance). The first principal components (PC) capture most of the variance in the data and generally have a repetitive and persistent structure, thus behaving approximately like the stationary component of the signal. In particular, coherent internal tides have significant spatial correlations that PCA could identify and isolate. On this basis, we believe that PCA applied to our total SLA can help better isolate the coherent internal tide (which is stationary) from the remaining residual tidal (incoherent internal tides) and non-tidal signals observed by SWOT. Egbert and Erofeeva (2021) have successfully used PCA to determine the characteristics of the incoherent internal tide around the Amazon shelf. In this paper we focus on the coherent internal tide. Therefore, we performed the PCA on the 104 cycles of the SWOT KaRin total SLA as defined in Equation 1. At each point in the swath, we filled in the missing value with the local time mean, then normalized the SLA to ensure that the global mean and standard deviation become zero and one respectively. The covariance matrix is calculated on the normalized SLA, the PCA focuses on eigenvalues and not absolute values.

The two leading PCA modes shown in Figure 7 account for 14.05% (PCA1, Figure 7a and c) and 10.46% (PCA2, Figure 7b and d) of the total variance. Their spatial patterns correspond to IT structures: on PCA1 (Figure 7a) the IT is intensified in area 1 and area 3, while PCA2 (Figure 7c) is characterized by

an increase of the IT intensity in area 2. PCs show 12–13 days oscillations with modulations around 70 days (Figure 7b and 7d), therefore recalling the aliasing periods of M2 and S2 waves (see table 1). To get a more precise idea of the wavelengths and frequencies contained in PCA1 and PCA2, we reconstructed the SLA for both components (SLA_pca1 and SLA_pca2) and calculated the spectra shown in Figure 8 (blue line for PCA1 and orange line for PCA2).
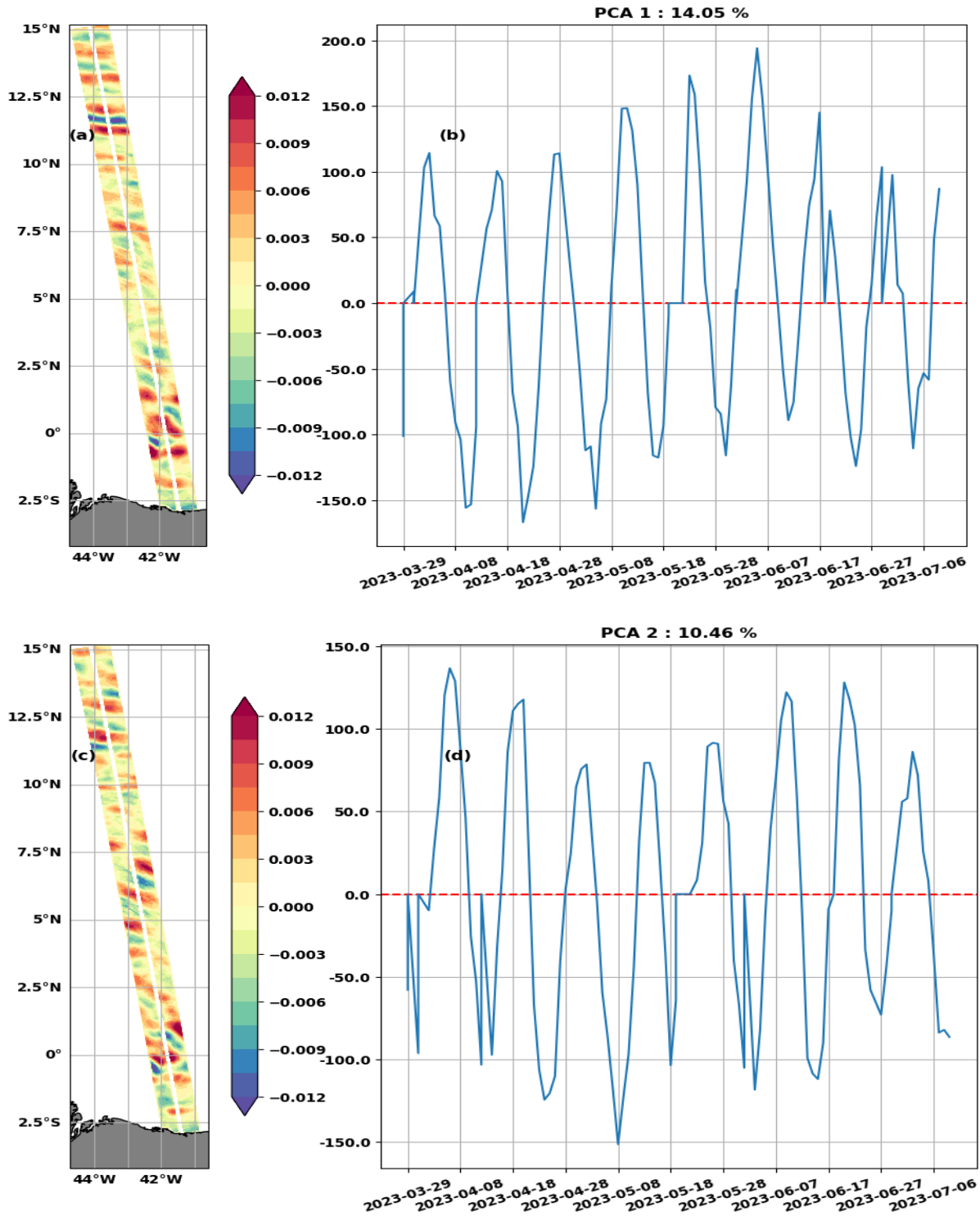
Figure 7: Spatial (left) and principal (right) components of PCA1 (top) and PCA2 (bottom) of the SLA along SWOT swaths over the Cal/Val period.

279   The wavenumber spectra (Figure 8a) indicate that PCA1 and PCA2 consist mainly of mode 1 (180-90
280   km) and mode 2 (80-60 km) IT. A peak that could be associated with mode 3 stands out on the PCA2
281   spectrum, but overall, the energy levels of both spectra remain low for higher modes (50-2 km). The
282   frequency spectra (Figure 8b) confirm that M2 is the dominant signal. At this frequency, the mean SLA
283   amplitudes are 0.52 cm for PCA1 and 0.45 cm for PCA2, respectively 71% and 61% of the 0.73 cm
284   associated with the peak of the total SLA reported by the solid black line in Figure 8b. Amplitudes are
285   low for other frequencies. The 104 available cycles are not enough to observe 70-days modulation on
286   the frequency spectra. Given the wavenumber and frequency spectra, we can say that PCA1 and PCA2
287   are two complementary representations of the propagation and evolution of the M2 dominant internal
288   tide, so they can be merged to form a single signal. We have summed SLA_pca1 and SLA_pca2 into
289   SLA_pca_L2 (L2 refers to lower or equal to 2). A snapshot of SLA_pca_L2 is shown in Figure 9a for the
290   same cycle as in Figure 2. Interestingly, the SLA reconstructed with PCA1 and PCA2 have similar
291   patterns to the mode 1 and mode 2 FFT-filtered SLAs (Figures 2b and 2c).

292   Between PCA3 and PCA10 the variance explained is less than 3.58% per PCA, from PCA11 onwards,
293   the variance becomes less than 2% (not shown). The PCs are a mixture of several wave frequencies,
294   with M2 of lower intensity than in PCA1 and PCA2, high frequency (faster than 10 days) and low
295   frequency (15, 17 or even 25 days). It is difficult to associate the spatial patterns of these PCAs with
296   the propagation of a persistent IT in time and along the track, or even with a mode of ocean variability
297   to our knowledge. The last 3 PCA patterns resemble residual noise from the processing of raw SWOT
298   data. We grouped PCA3 to PCA104 into SLA_pca_G2 (G2 for greater than 2). The small-scale structures
299   that were identified in Figure 2a are clearly visible in the snapshot of the SLA_pca_G2 in Figure 9b.
300   Figures 9a and 9b are complementary, as the PCA acted as a filter. The total SLA is now split into
301   SLA_pca_L2 and SLA_pca_G2. The spectra of SLA_pca_G2 are shown in green in Figure 8. Nearly all
302   energies for scales above 180 km (seen as large scale) and below 50 km (for higher modes) are found
303   in the wave number spectrum of SLA_pca_G2. Around the aliased frequency of M2, the mean
304   amplitude is 0.19 cm for SLA_pca_G2. This is about a quarter of the mean amplitude of the total SLA
305   (0.73 cm). With such a drop in the energy of the spectrum, it's tempting to say that separation by the
306   PCA has acted in the same way as a classical detiding. To verify this, we calculated the spectra of the
307   total SLA detided with M2 from ITkars and plotted them as a dashed black line in Figure 8. At all
308   frequencies and wavelengths, they overlap well with the spectra of SLA_pca_G2. Therefore,
309   SLA_pca_G2 is more representative of the incoherent internal tide and SLA_pca_L2 is more suitable
310   for improving the estimation of the coherent internal tide.

311

312

313

314
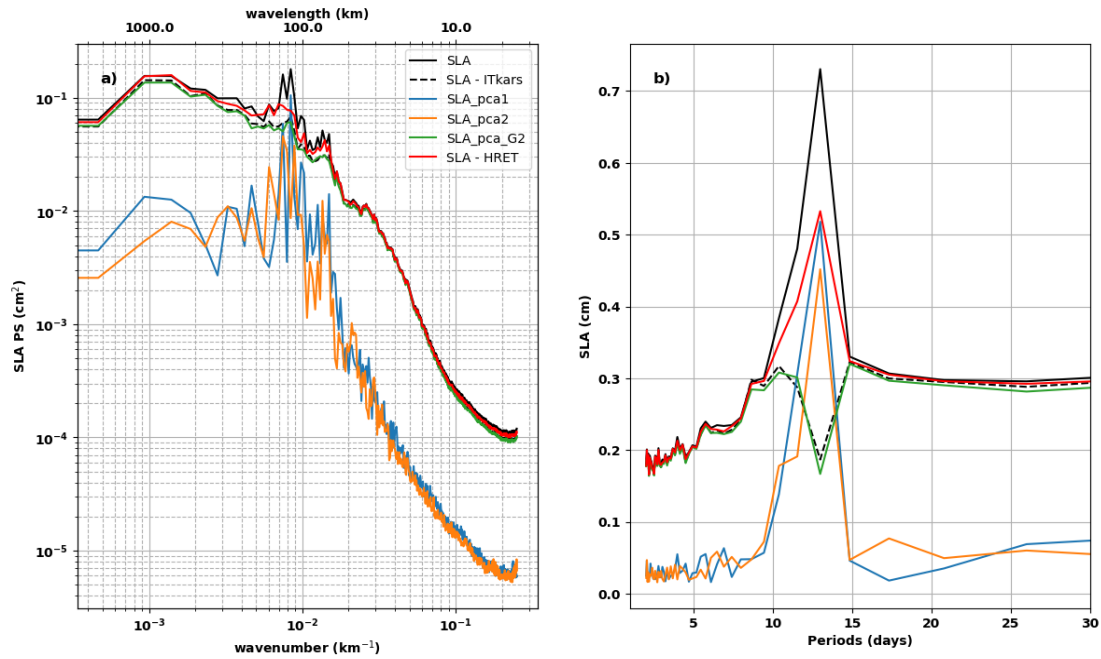
Figure 8: Wavenumber (a) and frequency (b) spectra of SLA_pca1 (in blue), SLA_pca2 (in orange),
SLA_pca_G2 (in green), SLA – HRET (in red) and SLA - ITkars (black dashed line). SLA_pca_G2 is the
sum of the SLAs of PCAs greater than 2. The spectra of total SLA (black solid line) from Figure 3 are
reported here. ITKars is the internal tide model derived from SWOT KaRIn data (cf in section 2).

319
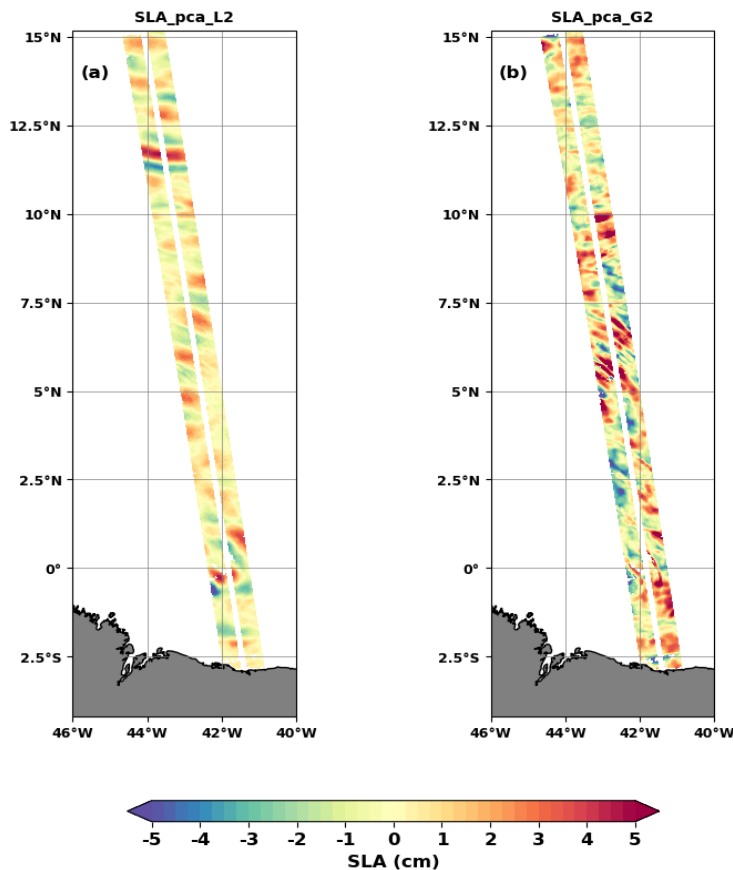
Figure 9: Snapshot of SWOT SLA_pca_L2 (a) and SLA_pca_G2 (b) on 08 April, 2023 (as in Figure 2).
SLA_pca_L2 is the sum of the SLAs of PCs less than or equal to 2 (PC1 and PC2).

322

3.2- ITkars_pca internal tide model

We have performed the harmonic analysis of SLA_pca_L2 at the semi-diurnal frequencies M2, N2 and S2 (Figure 10). The resulting internal tide amplitude (model) is referred to as ITkars_pca to distinguish it from ITkars based solely on harmonic analysis of SWOT Karin data. Compared to Figure 6 corresponding to ITkars, the ITkars_pca internal tide maps for N2 (Figure 10a) and S2 (Figure 10b) are cleared of small scales, and the patterns for both waves are now close to that of M2 as expected (Figure 10c and 5b reported in 10f). At first glance, there seems to be no difference between ITkars (Figure 5b or 10f) and ITkars_pca (Figure 10c) for M2. By making the complex difference between the two signals (Figure 10c and 10f), we deduce the amplitude shown in Figure 10d, which is equivalent to the amplitude of the harmonic analysis of SLA_pca_G2 at M2. As with N2 and S2, Figure 10d shows that M2 ITkars (Figure 5b or 10f) also contains an additional signal dominated by small scales, and which does not resemble the classic internal tide.

335
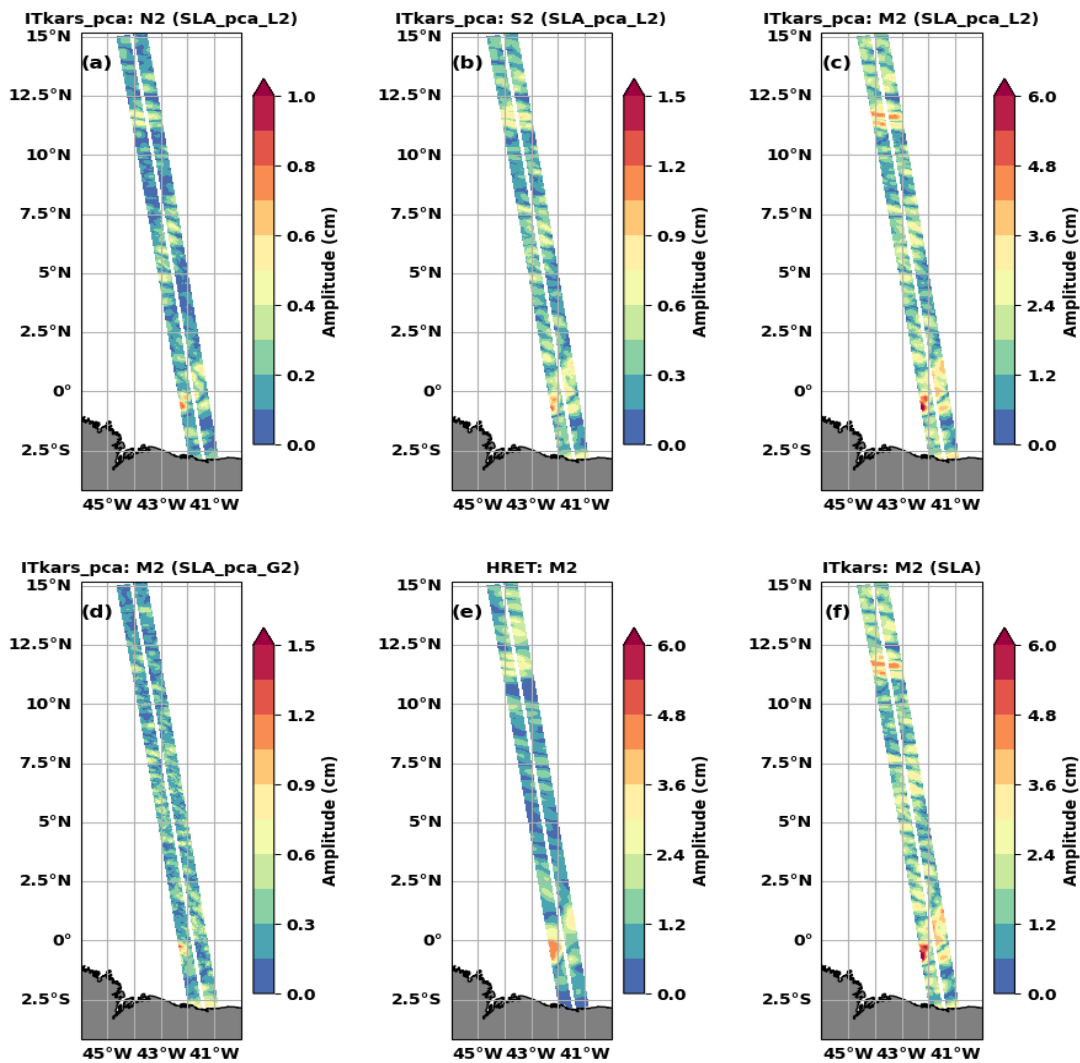
Figure 10: The amplitude (in cm) of the internal tides N2 (a), S2 (b) and M2 (c and d) of the ITkars_pca model derived by harmonic analysis of SLA_pca_L2 (a to c) and SLA_pca_G2 (d) over the Cal/Val period. SLA_pca_L2 is the SLA based on PCA1 and PCA2, SLA_pca_G2 is compiled from PCA3 to PCA104. Only swath points with at least 80 valid cycles were analyzed. Figure 5a and 5b are reported here, M2 HRET (e) and M2 ITkars (f).

The origin of the extra signal contaminating ITkars could be dynamic or numerical. Dynamically, these could be very intense non-linear waves, solitons, or incoherent internal tides, which are retained in the harmonic analysis of section 2 due to the short length of the time series. On the numerical side, noise linked to the pre-processing of SWOT data cannot be ruled out. Another source of contamination could also be the DUACS correction we apply beforehand to distinguish internal tides.

4 - Complementary comparison between SWOT and HRET IT models: predictability of internal tides

The comparison between HRET and SWOT based internal tides models (ITkars and ITkars_pca) is taken a step further in this final section. Each of the atlases (amplitude and phase) will be used as an internal tide correction model for the SWOT data. This involves making internal tide predictions over a given period and then subtracting these predictions from raw observations. Various metrics are used to quantify the capability of each model to reduce the variance.

In Figure 8, the ITkars M2 atlas has been used as a correction model to detide the total SLA over the entire Cal/Val observation period (black dashed line). We have done the same with M2 from HRET and the corresponding spectra is shown in red in Figure 8. As in figure 3, the 1D spectra are integrations of the 2D wavenumber-frequency spectrum. On the wavenumber spectra, the peaks of modes 1 and 2 are reduced but remain visible whatever the detiding applied (Figure 8a). We have integrated the wavenumber spectra of the total SLA (Black line in Figure 8) and the detided SLA (Black dashed and red line in Figure 8) over all wavelengths, between 180 and 90 km for mode 1, between 80 and 60 km for mode 2, from 50 to 2 km for the higher modes, and finally over wavelengths greater than 180 km for the large scale. The derived standard deviations are presented in Table 2 for the total SLA and the SLA detided with ITkars or HRET, as well as the percentages expressing the residual variance rate (ratio of the variances of the detided SLA on the total SLA). The higher is the standard deviation of the detided SLA or the percentage in Table 2, the less efficient is the correction used for detiding. According to Table 2, the application of the M2 internal tide prediction of each of the models removes very little variance from the SLA, nevertheless ITkars is more efficient than HRET especially at mode 1 and mode 2 scales. For these scales, the residual variance reaches 76% and 84% of the SLA after correction by ITkars and is likely to be incoherent internal tide. For the higher modes, Table 2 agrees with Figure 5e: the M2 correction has no effect on these scales. ITkars has a greater impact on large scale SLAs than HRET: HRET has almost no signal at large scale by construction, while ITkars can capture some variability at large scales due to short time-series and no fitting approximation. When detiding with ITkars, the energy spectrum (Figure 8b) decreases strongly around the aliased frequency of M2 (around 13 days, see Table 1). The mean of SLA amplitude along the SWOT swaths drops by 74% (from 0.73 cm to 0.19 cm) after ITkars detiding at M2 frequency. With the HRET correction (Figure 8), the peak amplitude at the M2 frequency is 0.53 cm, i.e. a 27% reduction of the peak of the total SLA, which is more than twice lower than with the ITkars correction. It can also be seen that periods of more than 15 days and less than 5 days are not affected by the correction, since we have limited ourselves to M2 frequency.

Table 2: Comparative table of the standard deviations of total SLA and SLA detided with HRET or ITkars. Standard deviations are obtained by integrating the spectra of Figure 3c on different wavelength bands (in cm). The ratio between detided SLA and total SLA, computed as a percentage, is given in parentheses.

	All wavelengths	Large scales >180km	Mode 1 180 - 90km	Mode 2 80 - 60km	Higher modes 50 - 2km
Total SLA	1.82	1.07	1.03	0.58	0.74
Detided	1.6 (88%)	0.99 (93%)	0.78 (76%)	0.49 (84%)	0.71 (96%)

ITkars					
Detided Hret	1.71 (94%)	1.04 (97%)	0.89 (86%)	0.54 (93%)	0.73 (99%)

382

383   The better performance of ITkars correction in comparison to HRET is not surprising, since ITkars is
384 derived from the same database to which the detiding is applied. The result is almost identical to ITkars
385 when the SLA is detided with M2 from ITkars_pca. This is not surprising as the amplitude of the M2
386 residual in SLA_pca_G2 is small (Figure 10d). To obtain the best possible comparison between ITkars
387 and ITkars_pca still focusing on M2 wave, we propose to apply the detiding to data that are
388 independent of those used to derive the internal tide atlas. Thus, the SWOT data were divided into
389 two periods: period 1, comprising the first 70 cycles (from late March to early June), and period 2 (from
390 early June to early July), comprising the last 34 cycles. We repeated the M2 harmonic analysis of the
391 total SLA over period 1 and derived the atlas "ITkars_p1" (p1 indicates period 1). We did the same with
392 SLA_pca_L2 and derived the atlas "ITkars_pca_p1". The atlases ITkars_p1, ITkars_pca_p1 and HRET are
393 then used to detide the SLA and SLA_pca_L2, first in period 1 and secondly in period 2, which is
394 independent of period 1. Since period 2 is short for frequency spectral analysis, we're going to look at
395 the standard deviation (Table 3) and the variance reduction (Figure 11). Variance reduction is
396 calculated from equation 2 as the difference between the variance of corrected SLA and the variance
397 of the uncorrected SLA (or SLA_pca_L2). A negative variance reduction indicates that the internal tide
398 correction reduces the SLA variance.

399   Variance reduction = var (SLA – M2 atlas) - var (SLA)   (2)

400 The spatial mean of the standard deviation is summarized in Table 3. On period 1, the standard
401 deviation of the total SLA is 2.56 cm. After correction with M2 of the HRET model, the standard
402 deviation drops by 7% (to 2.39 cm). The SLA standard deviation decreases by about 15% and 14% with
403 ITkars_p1 and ITkars_pca_p1, respectively. The difference between the two ITkars models is not
404 significant as we detide the same data that are used to derive the models (ITkarsp1 in particular). The
405 application of the corrections to SLA_pca_L2 reduces the residual standard deviation from 1.33 cm to
406 0.99 cm for HRET, to 0.53 cm for ITkars_p1 and to 0.42 cm for ITkars_pca_p1. This shows that even in
407 an SLA dominated by coherent internal tides, HRET removes only 15% of the variance, whereas SWOT-
408 based internal tide models remove over 60%. ITkars_pca_p1 is obviously the best correction for
409 SLA_pca_L2, with ITkars_p1 being slightly less efficient.

410   On period 2, the corrections of the SLA with the three internal tide models are less efficient. Table
411 3 shows that, on average, between 5% and 9% of the SLA variance is suppressed, with ITkars_pca_p1
412 being the best corrective internal tide model. As can be seen from the variance reduction maps (Figure
413 11a to c), the three models reduce variance (blue color) in the parts of the swath where the coherent
414 internal tide signal is strong enough (Figure 10). Outside these areas, the internal tide models tend to
415 add variance, and the variance reductions become positive. This undesirable effect of the correction
416 models is mainly observed in the central part of the swath (area 2), where the higher modes contribute
417 significantly to the SLA variability (see Figure 4). The effect in area 2 is pronounced for ITkars_p1 (Figure
418 11b), indicating a prediction failure. When considering the independent SLA_pca_L2 data (period 2,
419 Table 3), HRET removes 21% of the variance. For ITkars_p1 and ITkars_pca_p1, the variance is reduced
420 by 45% and 55% respectively. The impact of PCA on the derivation of the M2 internal tide atlas is
421 highlighted here by the 10% gap between the percentages of variance reduction when applying the
422 two models based on SWOT observations. The variance reduction figures confirm that the correction
423 works better on SLA_pca_L2 (Figure 11 d to e). Although there are still swath locations with positive

variance reduction, this is no longer concentrated in the central part. Variance reductions are dominated by negative values for ITkars_p1 (Figure 11e) and ITkars_pca_p1 (Figure 11f).

Table3: Comparative table of standard deviations (cm) of SLA and SLA_pca_L2 detided with either M2 HRET, M2 ITkars or M2 ITkars_pca models over period 1 (from late March to early June 2023, the first 70 cycles) and period 2 (from early June to early July 2023, the last 34 cycles). ITkars_p1 and ITkar_pca_p1 models were built on period 1 and validated on period 2. The ratio between detided SLA and total SLA is indicated in the parentheses (in percent).

	Period 1		Period 2	
	SLA	SLA_pca_L2	SLA	SLA_pca_L2
no IT correction	2.56	1.33	2.79	1.15
HRET	2.39 (93%)	0.99 (74%)	2.64 (95%)	0.91 (79%)
ITkars_p1	2.18 (85%)	0.53 (40%)	2.65 (95%)	0.63 (55%)
ITkars_pca_p1	2.21 (86%)	0.42 (32%)	2.55 (91%)	0.52 (45%)
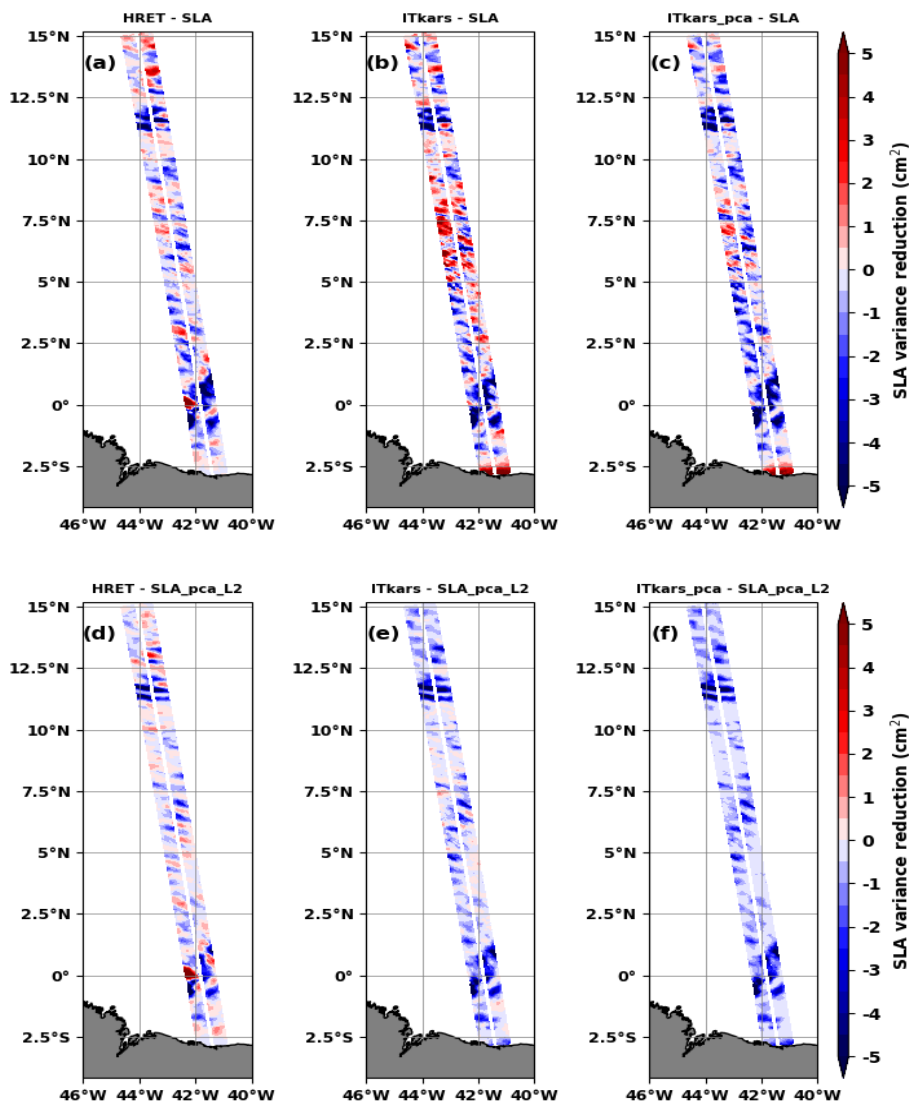
Figure 11: Variance reduction (in cm²) on period 2 from early June to early July (last 34 cycles) when using either M2 HRET (left column) or M2 ITkars_p1 (middle column) or M2 ITkars_pca_p1 (right column) to correct the total SLA (top line) or SLA_pca_L2 (bottom line).

436

437

4- Discussion and perspectives

In this study, we explored and characterized the internal tide signal in SWOT KaRIn observations over the Cal/Val period (1-day orbit) between late March and early July 2023 (104 cycles) and along the track 20 located off the Amazon shelf in the tropical Atlantic between 2°S and 15°N. The internal tide as seen by SWOT is a mixture of several spatial scales, including baroclinic modes 1 and 2 defined by wavelengths between 180-90 km and 80-60 km respectively. SWOT also sees very intense fine-scale structures (wavelengths between 50-2 km) that we have associated with higher baroclinic modes, including modes 3, 4 and 5 according to Barbot et al., (2021). As a result, SWOT seems to live up to expectations, providing a direct 2D view of the internal tide sea surface signatures and even access to smaller scales.

Our approach to extract the internal tide signal through the 1-day SWOT data consisted firstly of filtering the large scale (including the mesoscale) by subtracting the DUACS MSLA from the SWOT observations; then we reintroduced the internal tide correction HRET from Zaron (2019) to obtain a SLA consisting of the total internal tide signal. We either performed the harmonic analysis (as in section 2) or proceeded upstream to the PCA before the harmonic analysis (as in section 3). The internal tide model based on harmonic analysis of SWOT KaRin data was referenced ITkars (Internal Tide from KaRin Swot), the one obtained by combining PCA and harmonic analysis ITkars_pca. We focused on the semi-diurnal frequencies M2, S2 and N2.

Spatial patterns of M2 internal tides from ITkars and ITkars_pca models agreed with the M2 HRET model based on nearly 25 years of conventional altimeter (nadir) observations. The similarities between models based on SWOT Karin and model with conventional altimeter are partly linked to the fact that SWOT data are analyzed over March to July during which the internal tide is most stable and coherent off the Amazon shelf (Tchilibou et al., 2022). One consequence of analyzing SWOT data over this short 104-day window is that the amplitude of the internal tide is stronger with SWOT estimation than with HRET. This result is logical since the intensity of the coherent internal tide depends on the length of the time series analyzed: a longer time series allows a better estimate of the coherent signal which is therefore smoother (Ansong et al.,2015; Zhou et al.,2015; Nash et al.,2012). The separation of M2 from O1 is not ensured with 104 cycles of SWOT 1-day data, however, in this region the amplitude of the internal tide is negligible at O1 frequency compared to M2 (see Figure 1 in Tchilibou et al.,2022), so M2 ITkars_pca is thus quite reliable.

The maps of N2 and S2 highlight the contamination of ITkars by signals other than the coherent internal tide, and particularly by very small scales. We hypothesize that the contamination is due to the leakage of nonlinear waves, incoherent internal tides, and ocean variability in the harmonic analyses. Regarding ocean variability, part of it is not captured by DUACS and was therefore not subtracted from the SLA. Moreover, subtracting the mesoscale, as we have done, is itself a possible source of error in estimating the internal tide (Zaron and Ray, 2018). One way to reduce the effects of contamination by ocean circulation would be to apply a simultaneous internal tide and mesoscale inversion method as proposed by Ubelmann et al. (2022). The combination of PCA and harmonic analysis gives semi-diurnal ITkars_pca maps (M2, S2 and N2) with similar patterns. The amplitude of N2 ITkars_pca deduced from SWOT is of the same order as that in the new product HRET14 (Zaron and Elipot 2024). The result is encouraging for S2, especially as the length of the 1-day observations is not sufficient to correctly separate it from waves such as Sa and Ssa, whose periods are identical to those of the annual and semi-annual variation of the ocean. A longer time series is needed to better separate

481 the internal tide components from SWOT observation, and we will consider analyses of the 21-day
482 SWOT science orbit data when the time series will be long enough.

483   PCA has improved our estimate of the internal tide model from the SWOT KaRin data. From the
484 PCA we kept the first two main modes (PCA1 and PCA2) and considered them as the coherent internal
485 tide given their fairly stationary character. Thus, the coherent internal tide accounts for 24.51% (14.05
486 of PCA1 and 10.46 of PCA2) of SLA variance in 1-day SWOT observations, a proportion in line with the
487 studies of Zaron (2017) and Egbert and Erofeeva (2021) in this region. The coherent internal tide
488 isolated through the PCA consists of mode1, mode 2 noticeable in PCA1 and PCA2. The fact that the
489 coherent internal tide signal is projected onto two main modes of the PCA is an open question. The
490 principal components of PCA1 and PCA2 are shifted by 3 to 4 days, about a quarter of the aliased
491 frequency of M2, which could correspond to a phase quadrature, as there is between the imaginary
492 and real parts needed to reconstruct a sinusoidal signal. Instead of being the real and imaginary parts
493 of a signal, PCA1 and PCA2 could also represent the same phenomenon and highlight its evolution in
494 area 2 in the middle of the swaths: the moderation of internal tides in area 2 with PCA1 and their
495 intensification with PCA2. This type of PCA/EOF behavior is observed in the case of ENSO studies in the
496 Pacific (Takahashi et al., 2011). The peaks on the wave number spectrum of PCA1 and PCA2 are shifted
497 by few kilometers at the mode 1 and mode 2 scales, suggesting a change in wavelengths relating to
498 changes in stratification conditions as suggested by Barbot et al. (2021). A longer series of Cal/Val
499 observations could have helped to better distinguish PCA1 from PCA2.

500   The principal components (time series) of PCA1 and PCA2 provide an overview and an opportunity
501 to study the daily variability of internal tide amplitude, a perspective difficult to access with
502 conventional altimetry missions. This opportunity to learn more about the temporal variability of the
503 internal tide using a single high-resolution mission is lost, or at least postponed, with SWOT's switch
504 to its 21-days scientific orbit. One of the limitations of using PCA to analyze SWOT data is probably its
505 sensitivity to track length. The total variance is distributed differently in the principal components
506 depending on whether the track is long or short, or whether ocean dynamics change significantly along
507 the track. It would be interesting to look at this point in the perspective of a global model, for example.
508 We are curious to know how the PCA will behave in the case of multi-track use, and at their crossing
509 points.

510   In the context of 1-day SWOT observations, the use of PCA can be useful in determining wave
511 frequencies of interest for the development of the coherent internal tide model. The combination of
512 PCA and harmonic analysis further reveals the observational potential of SWOT. We are currently
513 working on other SWOT tracks in various ocean regions to test the robustness of our method
514 combining PCA and harmonic analysis. We also plan to explore in situ observations of the SWOT Cal/Val
515 and other databases to understand better our results. Work remains to be done to confirm the
516 presence of mode 3 in the coherent internal tide signal in this region. The incoherence of the internal
517 tide and its interaction with the circulation are other issues to be addressed with these SWOT data.

518   The final issue addressed in this study was the correction of the internal tide signal in the SWOT 1-
519 day observations. On average, the HRET model corrects only 6% of the SLA variance over the Cal/Val
520 period, while ITkars based on SWOT observations corrects 12% (Table 2). These percentages are low
521 due to the high degree of internal tides incoherency in this part of the ocean. However, they indicate
522 that the HRET correction is not efficient enough. It would be more relevant to directly evaluate the
523 internal tide signals on 1-day SWOT observations and then use it as a correction model. The harmonic
524 analysis may be sufficient if the aim is to apply the tidal model to the same data, but if not, the previous
525 step of the PCA is recommended to obtain a more realistic model. The question of correcting internal

526 tides and improving internal tide models will also remain a challenge for the exploitation of SWOT's
527 21-day cycles.

528

529 **Authors contributions:** This work is part of the Marée - SWOT project funded by the CNES at CLS. MT's
530 work and analyses are supervised by LC and FL. Conceptualization: TM, LC, FL, CU. MT wrote the
531 paper with contributions from all co-authors.

532 **Competing interests:** The contact author has declared that none of the authors has any
533 competing interests
534

535 **References:**

536 Aguedjou, H. M. A., Dadou, I., Chaigneau, A., Morel, Y., and Alory, G.: Eddies in the Tropical Atlantic
537 Ocean and Their Seasonal Variability, Geophysical Research Letters, 46, 12156–12164,
538 https://doi.org/10.1029/2019GL083925, 2019.

539 Alford, M. H., Peacock, T., MacKinnon, J. A., Nash, J. D., Buijsman, M. C., Centurioni, L. R., Chao, S.-Y.,
540 Chang, M.-H., Farmer, D. M., Fringer, O. B., Fu, K.-H., Gallacher, P. C., Graber, H. C., Helfrich, K. R.,
541 Jachec, S. M., Jackson, C. R., Klymak, J. M., Ko, D. S., Jan, S., Johnston, T. M. S., Legg, S., Lee, I.-H., Lien,
542 R.-C., Mercier, M. J., Moum, J. N., Musgrave, R., Park, J.-H., Pickering, A. I., Pinkel, R., Rainville, L., Ramp,
543 S. R., Rudnick, D. L., Sarkar, S., Scotti, A., Simmons, H. L., St Laurent, L. C., Venayagamoorthy, S. K.,
544 Wang, Y.-H., Wang, J., Yang, Y. J., Paluszkiewicz, T., and (David) Tang, T.-Y.: The formation and fate of
545 internal waves in the South China Sea, Nature, 521, 65–69, https://doi.org/10.1038/nature14399,
546 2015.

547 Ansong, J. K., Arbic, B. K., Buijsman, M. C., Richman, J. G., Shriver, J. F., and Wallcraft, A. J.: Indirect
548 evidence for substantial damping of low-mode internal tides in the open ocean, JGR Oceans, 120,
549 6057–6071, https://doi.org/10.1002/2015JC010998, 2015.

550 Arbic, B., Richman, J., Shriver, J., Timko, P., Metzger, J., and Wallcraft, A.: Global Modeling of Internal
551 Tides Within an Eddying Ocean General Circulation Model, oceanog, 25, 20–29,
552 https://doi.org/10.5670/oceanog.2012.38, 2012.

553 Assene, F., Koch-Larrouy, A., Dadou, I., Tchilibou, M., Morvan, G., Chanut, J., Costa Da Silva, A.,
554 Vantrepotte, V., Allain, D., and Tran, T.-K.: Internal tides off the Amazon shelf – Part 1: The importance
555 of the structuring of ocean temperature during two contrasted seasons, Ocean Sci., 20, 43–67,
556 https://doi.org/10.5194/os-20-43-2024, 2024.

557 Bai, X., Lamb, K. G., and Da Silva, J. C. B.: Small-Scale Topographic Effects on the Generation of Along-
558 Shelf Propagating Internal Solitary Waves on the Amazon Shelf, JGR Oceans, 126, e2021JC017252,
559 https://doi.org/10.1029/2021JC017252, 2021.

560 Ballarotta, M., Ubelmann, C., Veillard, P., Prandi, P., Etienne, H., Mulet, S., Faugère, Y., Dibarboure, G.,
561 Morrow, R., and Picot, N.: Improved global sea surface height and current maps from remote sensing
562 and in situ observations, Earth Syst. Sci. Data, 15, 295–315, https://doi.org/10.5194/essd-15-295-2023,
563 2023.

564 Ballarotta, M., Ubelmann, C., Pujol, M.-I., Taburet, G., Fournier, F., Legeais, J.-F., Faugère, Y.,
565 Delepoulle, A., Chelton, D., Dibarboure, G., and Picot, N.: On the resolutions of ocean altimetry maps,
566 Ocean Sci., 15, 1091–1109, https://doi.org/10.5194/os-15-1091-2019, 2019.

567 Barbot, S., Lyard, F., Tchilibou, M., and Carrere, L.: Background stratification impacts on internal tide

generation and abyssal propagation in the western equatorial Atlantic and the Bay of Biscay, Ocean Sci., 17, 1563–1583, https://doi.org/10.5194/os-17-1563-2021, 2021.

Brandt, P., Rubino, A., and Fischer, J.: Large-Amplitude Internal Solitary Waves in the North Equatorial Countercurrent, J. Phys. Oceanogr., 32, 1567–1573, https://doi.org/10.1175/1520-0485(2002)032<1567:LAISWI>2.0.CO;2, 2002.

Buijsman, M. C., Arbic, B. K., Richman, J. G., Shriver, J. F., Wallcraft, A. J., and Zamudio, L.: Semidiurnal internal tide incoherence in the equatorial Pacific, JGR Oceans, 122, 5286–5305, https://doi.org/10.1002/2016JC012590, 2017.

Carrere, L., Arbic, B. K., Dushaw, B., Egbert, G., Erofeeva, S., Lyard, F., Ray, R. D., Ubelmann, C., Zaron, E., Zhao, Z., Shriver, J. F., Buijsman, M. C., and Picot, N.: Accuracy assessment of global internal-tide models using satellite altimetry, Ocean Sci., 17, 147–180, https://doi.org/10.5194/os-17-147-2021, 2021.

Chelton, D. B., Schlax, M. G., and Samelson, R. M.: Global observations of nonlinear mesoscale eddies, Progress in Oceanography, 91, 167–216, https://doi.org/10.1016/j.pocean.2011.01.002, 2011.

De Macedo, C. R., Koch-Larrouy, A., Da Silva, J. C. B., Magalhães, J. M., Lentini, C. A. D., Tran, T. K., Rosa, M. C. B., and Vantrepotte, V.: Spatial and temporal variability in mode-1 and mode-2 internal solitary waves from MODIS-Terra sun glint off the Amazon shelf, Ocean Sci., 19, 1357–1374, https://doi.org/10.5194/os-19-1357-2023, 2023.

Dibarboure, G., Anadon, C., Briol, F., Cadier, E., Chevrier, R., Delepoulle, A., Faugère, Y., Laloue, A., Morrow, R., Picot, N., Prandi, P., Pujol, M.-I., Raynal, M., Treboutte, A., and Ubelmann, C.: Blending 2D topography images from SWOT into the altimeter constellation with the Level-3 multi-mission DUACS system, EGUsphere [preprint], https://doi.org/10.5194/egusphere-2024-1501, 2024.

Duda, T. F., Lin, Y.-T., Buijsman, M., and Newhall, A. E.: Internal Tidal Modal Ray Refraction and Energy Ducting in Baroclinic Gulf Stream Currents, Journal of Physical Oceanography, 48, 1969–1993, https://doi.org/10.1175/JPO-D-18-0031.1, 2018.

Dufau, C., Orsztynowicz, M., Dibarboure, G., Morrow, R., and Le Traon, P.: Mesoscale resolution capability of altimetry: Present and future, JGR Oceans, 121, 4910–4927, https://doi.org/10.1002/2015JC010904, 2016.

Dunphy, M. and Lamb, K. G.: Focusing and vertical mode scattering of the first mode internal tide by mesoscale eddy interaction, JGR Oceans, 119, 523–536, https://doi.org/10.1002/2013JC009293, 2014.

Dunphy, M., Ponte, A. L., Klein, P., and Le Gentil, S.: Low-Mode Internal Tide Propagation in a Turbulent Eddy Field, Journal of Physical Oceanography, 47, 649–665, https://doi.org/10.1175/JPO-D-16-0099.1, 2017.

Dushaw,B. D: An Empirical Model for Mode-1 Internal Tides Derived from Satellite Altimetry: Computing Accurate Tidal Predictions at Arbitrary Points over the World oceans, Technical Memorandum APL-UW TM: https://apl.uw.edu/project/project.php?id=tm_1-15, (last access: 2 June 2024), 2015.

Egbert, G. D. and Erofeeva, S. Y.: An Approach to Empirical Mapping of Incoherent Internal Tides With Altimetry Data, Geophysical Research Letters, 48, e2021GL095863, https://doi.org/10.1029/2021GL095863, 2021.

608 Fu, L.-L. and Ubelmann, C.: On the Transition from Profile Altimeter to Swath Altimeter for Observing
609 Global Ocean Surface Topography, Journal of Atmospheric and Oceanic Technology, 31, 560–568,
610 https://doi.org/10.1175/JTECH-D-13-00109.1, 2014.

611 Fu, L.-L., Alsdorf, D., Rodriguez, E., Morrow, R., Mognard, N., Lambin, J., Vaze, P., and Lafon, T.: THE
612 SURFACE WATER AND OCEAN TOPOGRAPHY (SWOT) MISSION, California, CA: JPL publication, 2012.

613 Gill, A. E.: Atmosphere-ocean dynamics, Nachdr., Acad. Press, San Diego, 662 pp., 2006.

614 Jackson, C., Da Silva, J., and Jeans, G.: The Generation of Nonlinear Internal Waves, oceanog, 25, 108–
615 123, https://doi.org/10.5670/oceanog.2012.46, 2012.

616 Jolliffe, I. T.: Principal Component Analysis, Springer New York, New York, NY,
617 https://doi.org/10.1007/978-1-4757-1904-8, 1986.

618 Kelly, S. M.: The Vertical Mode Decomposition of Surface and Internal Tides in the Presence of a Free
619 Surface and Arbitrary Topography, Journal of Physical Oceanography, 46, 3777–3788,
620 https://doi.org/10.1175/JPO-D-16-0131.1, 2016.

621 Le Guillou, F., Lahaye, N., Ubelmann, C., Metref, S., Cosme, E., Ponte, A.: Joint estimation of balanced
622 motions and internal tides from future wide-swath altimetry. Journal of Advances in Modeling Earth
623 Systems, 13(12), e2021MS002613. https://doi.org/10.1029/2021ms002613, 2021.

624 Le Provost, C.: Chapter 6 Ocean Tides, in: International Geophysics, vol. 69, Elsevier, 267–303,
625 https://doi.org/10.1016/S0074-6142(01)80151-0, 2001.

626 Lentini, C., Magalhães, J., Da Silva, J., and Lorenzzetti, J.: Transcritical Flow and Generation of Internal
627 Solitary Waves off the Amazon River: Synthetic Aperture Radar Observations and Interpretation,
628 Oceanog., 29, 187–195, https://doi.org/10.5670/oceanog.2016.88, 2016.

629 Lyard, F. H., Allain, D. J., Cancet, M., Carrere, L., and Picot, N.: FES2014 global ocean tide atlas: design
630 and performance, Ocean Sci., 17, 615–649, https://doi.org/10.5194/os-17-615-2021, 2021.

631 Magalhaes, J. M., Da Silva, J. C. B., Buijsman, M. C., and Garcia, C. A. E.: Effect of the North Equatorial
632 Counter Current on the generation and propagation of internal solitary waves off the Amazon shelf
633 (SAR observations), Ocean Sci., 12, 243–255, https://doi.org/10.5194/os-12-243-2016, 2016.

634 Morrow, R., Fu, L.-L., Ardhuin, F., Benkiran, M., Chapron, B., Cosme, E., d'Ovidio, F., Farrar, J. T., Gille,
635 S. T., Lapeyre, G., Le Traon, P.-Y., Pascual, A., Ponte, A., Qiu, B., Rascle, N., Ubelmann, C., Wang, J., and
636 Zaron, E. D.: Global Observations of Fine-Scale Ocean Surface Topography With the Surface Water and
637 Ocean Topography (SWOT) Mission, Front. Mar. Sci., 6, 232,
638 https://doi.org/10.3389/fmars.2019.00232, 2019.

639 Nash, J., Shroyer, E., Kelly, S., Inall, M., Duda, T., Levine, M., Jones, N., and Musgrave, R.: Are Any
640 Coastal Internal Tides Predictable?, oceanog, 25, 80–95, https://doi.org/10.5670/oceanog.2012.44,
641 2012.

642 Nelson, A. D., Arbic, B. K., Zaron, E. D., Savage, A. C., Richman, J. G., Buijsman, M. C., and Shriver, J. F.:
643 Toward Realistic Nonstationarity of Semidiurnal Baroclinic Tides in a Hydrodynamic Model, JGR
644 Oceans, 124, 6632–6642, https://doi.org/10.1029/2018JC014737, 2019.

645 Niwa, Y. and Hibiya, T.: Estimation of baroclinic tide energy available for deep ocean mixing based on
646 three-dimensional global numerical simulations, J Oceanogr, 67, 493–502,

647 https://doi.org/10.1007/s10872-011-0052-1, 2011.

648 Ponte, A. L. and Klein, P.: Incoherent signature of internal tides on sea level in idealized numerical
649 simulations, Geophysical Research Letters, 42, 1520–1526, https://doi.org/10.1002/2014GL062583,
650 2015.

651 Ray, R. D. and Mitchum, G. T.: Surface manifestation of internal tides in the deep ocean: observations
652 from altimetry and island gauges, Progress in Oceanography, 40, 135–162,
653 https://doi.org/10.1016/S0079-6611(97)00025-6, 1997.

654 Savage, A. C., Waterhouse, A. F., and Kelly, S. M.: Internal Tide Nonstationarity and Wave–Mesoscale
655 Interactions in the Tasman Sea, Journal of Physical Oceanography, 50, 2931–2951,
656 https://doi.org/10.1175/JPO-D-19-0283.1, 2020.

657 Solano, M. S., Buijsman, M. C., Shriver, J. F., Magalhaes, J., Da Silva, J., Jackson, C., Arbic, B. K., and
658 Barkan, R.: Nonlinear Internal Tides in a Realistically Forced Global Ocean Simulation, JGR Oceans, 128,
659 e2023JC019913, https://doi.org/10.1029/2023JC019913, 2023.

660 St. Laurent, L. and Garrett, C.: The Role of Internal Tides in Mixing the Deep Ocean, J. Phys. Oceanogr.,
661 32, 2882–2899, https://doi.org/10.1175/1520-0485(2002)032<2882:TROITI>2.0.CO;2, 2002.

662 Takahashi, K., Montecinos, A., Goubanova, K., and Dewitte, B.: ENSO regimes: Reinterpreting the
663 canonical and Modoki El Niño: REINTERPRETING ENSO MODES, Geophys. Res. Lett., 38, n/a-n/a,
664 https://doi.org/10.1029/2011GL047364, 2011.

665 Tchilibou, M., Gourdeau, L., Lyard, F., Morrow, R., Koch Larrouy, A., Allain, D., and Djath, B.: Internal
666 tides in the Solomon Sea in contrasted ENSO conditions, Ocean Sci., 16, 615–635,
667 https://doi.org/10.5194/os-16-615-2020, 2020.

668 Tchilibou, M., Koch-Larrouy, A., Barbot, S., Lyard, F., Morel, Y., Jouanno, J., and Morrow, R.: Internal
669 tides off the Amazon shelf during two contrasted seasons: interactions with background circulation
670 and SSH imprints, Ocean Sci., 18, 1591–1618, https://doi.org/10.5194/os-18-1591-2022, 2022.

671 Ubelmann, C., Dibarboure, G., Gaultier, L., Ponte, A., Ardhuin, F., Ballarotta, M., and Faugère, Y.:
672 Reconstructing Ocean Surface Current Combining Altimetry and Future Spaceborne Doppler Data, JGR
673 Oceans, 126, e2020JC016560, https://doi.org/10.1029/2020JC016560, 2021.

674 Ubelmann, C., Carrere, L., Durand, C., Dibarboure, G., Faugère, Y., Ballarotta, M., Briol, F., and Lyard,
675 F.: Simultaneous estimation of ocean mesoscale and coherent internal tide sea surface height
676 signatures from the global altimetry record, Ocean Sci., 18, 469–481, https://doi.org/10.5194/os-18-
677 469-2022, 2022.

678 Ubelmann, C., P. Klein, and L.-L. Fu: Dynamic interpolation of sea surface height and potential
679 applications for future high-resolution altimetry mapping. J. Atmos. Ocean. Technol., 32, 177–184,
680 https://doi.org/10.1175/JTECH-D-14-00152.1, 2015

681 Vic, C., Naveira Garabato, A. C., Green, J. A. M., Waterhouse, A. F., Zhao, Z., Melet, A., De Lavergne, C.,
682 Buijsman, M. C., and Stephenson, G. R.: Deep-ocean mixing driven by small-scale internal tides, Nat
683 Commun, 10, 2099, https://doi.org/10.1038/s41467-019-10149-5, 2019.

684 Wang, H., Grisouard, N., Salehipour, H., Nuz, A., Poon, M., & Ponte, A. L.: A deep learning approach
685 to extract internal tides scattered by geostrophic turbulence. Geophysical Research
686 Letters, 49, e2022GL099400. https://doi.org/10.1029/2022GL099400, 2022.

687 Wang, J. and Fu, L.-L.: On the Long-Wavelength Validation of the SWOT KaRIn Measurement, Journal
688 of Atmospheric and Oceanic Technology, 36, 843–848, https://doi.org/10.1175/JTECH-D-18-0148.1,
689 2019.

690 Zaron E. D. and S. Elipot: Estimates of Baroclinic Tidal Sea Level and Currents from Lagrangian Drifters
691 and Satellite Altimetry, Journal of Atmospheric and Oceanic Technology, 41, 781-802
692 https://doi.org/10.1175/JTECH-D-23-0159.1, 2024.

693 Zaron, E. D.: Mapping the nonstationary internal tide with satellite altimetry, JGR Oceans, 122, 539–
694 554, https://doi.org/10.1002/2016JC012487, 2017.

695 Zaron, E. D.: Baroclinic Tidal Sea Level from Exact-Repeat Mission Altimetry, Journal of Physical
696 Oceanography, 49, 193–210, https://doi.org/10.1175/JPO-D-18-0127.1, 2019.

697 Zaron, E. D. and Ray, R. D.: Aliased Tidal Variability in Mesoscale Sea Level Anomaly Maps, Journal of
698 Atmospheric and Oceanic Technology, 35, 2421–2435, https://doi.org/10.1175/JTECH-D-18-0089.1,
699 2018.

700 Zhao, Z.: Mapping Internal Tides from Satellite Altimetry Without Blind Directions, JGR Oceans, 124,
701 8605–8625, https://doi.org/10.1029/2019JC015507, 2019.

702 Zhao, Z.: Seasonal mode-1 M2 internal tides from satellite altimetry, Journal of Physical Oceanography,
703 https://doi.org/10.1175/JPO-D-21-0001.1, 2021.

704 Zhou, X., Wang, D., and Chen, D.: Validating satellite altimeter measurements of internal tides with
705 long-term TAO/TRITON buoy observations at 2°S–156°E, Geophysical Research Letters, 42, 4040–4046,
706 https://doi.org/10.1002/2015GL063669, 2015.

707

708

709

710

711

712

713

714

715

716